Received: Added at production | Revised: Added at production | Accepted: Added at production

DOI: xxx/xxxx

RESEARCH ARTICLE

A digital twin of atomic ensemble quantum memories

Elizabeth Jane Robertson[†1] | **Benjamin Maaß**[†1] | **Konrad Tschernig**[1] | **Janik Wolters**[1,2,3,4]

[1]Institute of Space Research, German Aerospace Center (DLR), Berlin, Germany

[2]Institutes of Physics, Technische Universiåt Berlin, Berlin, Germany

[3]Einstein Center Digital Future (ECDF) Berlin, Germany

[4]AQLS UG Haftungsbeschränkt, Germany

Correspondence
Corresponding author: Elizabeth Jane Robertson
Email: elizabeth.robertson@dlr.de

Present address
Rutherfordstr. 2, 12489 Berlin

Abstract

Accurate performance estimation of experimentally demonstrated quantum memories is key to understand the nuances in their deployment in photonic quantum networks. While several software packages allow for accessible quantum simulation, they often do not account for the loss and noise in physical devices. We present a framework for modeling ensemble-based atomic quantum memories using the quantum channel formalism. We provide a Kraus matrix representation of several experimentally implemented state-of-the art quantum memories and give an overview of their most important performance metrics. To showcase the applicability of this approach, we implement a memory-assisted quantum token protocol within our simulation framework. Our digital twin model is readily extensible to other memory implementations and easily compatible with existing frameworks for performance simulation of experimental quantum networks.

KEYWORDS
quantum memory, quantum network, digital twin, performance simulation

1 | INTRODUCTION

The vision of a quantum internet [1] has driven quantum technology research over the last decades. The backbone of such a network is entanglement distribution between remote network nodes that are connected via photonic quantum channels [2]. However, optical losses in fibers severely limit the possible scale of entanglement distribution and create the need for quantum repeaters. In this context, quantum memories are critical components of any repeater-based transfer of quantum information. Their application in buffering, synchronizing and conditioning of photonic quantum information requires an in-depth knowledge of the inner workings of quantum memories [3, 4]. Equally as important is the ability to understand the performance of different quantum memory platforms, experimental implementations and compatibilities with other photonic resources, all within the context of multi-layered network architectures.

Theoretical investigations of ensemble-based quantum memories on the one hand are well-established [5, 6] but often remain very specialized in their scope. On the other hand, recent years have shown remarkable progress in the development of tool-kits for photonic quantum simulation. Prominently, *Strawberry fields* [7], *Perceval* [8] and *Piquasso* [9] have emerged as tools for Gaussian- and discrete Boson sampling and photonic quantum computing. In addition, tools for simulating open quantum systems *QuTiP*[10] and gate-based computing *Qiskit*[11] with extension module for optics *SOQCS*[12] have been published. However, there is a lack of open source, close-to-experiment plug-and-play software packages to simulate real quantum communication devices taking into account noise, loss and decoherence processes which requires significant manual customization in presently available simulation frameworks.

In this work we develop a general model of atomic ensemble-based quantum memories, taking loss-, noise- and decoherence processes into account, and demonstrate the plug-and-play software implementation in several test-scenarios. First, we describe the basic working principle of ensemble-based quantum memories and introduce their most important performance characteristics 2. Second, after introducing the description of a quantum memory within the channel formalism 3 we demonstrate the functionality of the simulation and apply it in a Mach-Zehnder configuration. Furthermore, we introduce simulation building blocks as digital twins of state-of-the-art vapor memories which allows for straightforward performance comparisons. Finally,

[†] The authors contributed equally to this work.

we apply the digitally twined memories to a quantum token protocol and benchmark the memory performances against the security of the protocol 5.

2 | QUANTUM MEMORIES

Fundamentally, a memory is a device that stores some type of information encoded in a propagating or short-lived state. The information is transferred to a storage medium by encoding it in a long-lived storage state and retrieved at a later time with a certain efficiency and fidelity. The term efficiency refers to the probability of a successful memory operation versus the number of trials. The fidelity of a memory is defined as the similarity between the input and the retrieved information. In the case of quantum states to be stored the re-encoding of information in a storage medium is fundamentally difficult as it entails a projective measurement of the quantum state which changes the properties of the state itself. Specifically, an unknown quantum state cannot be reconstructed from a single measurement. Crucially, this means that storing quantum information requires storing the *entire* state and not only its projections onto some measurement basis during the storage process. The challenge in constructing such a system lies in the fundamental impossibility to create identical copies of arbitrary quantum states[13].

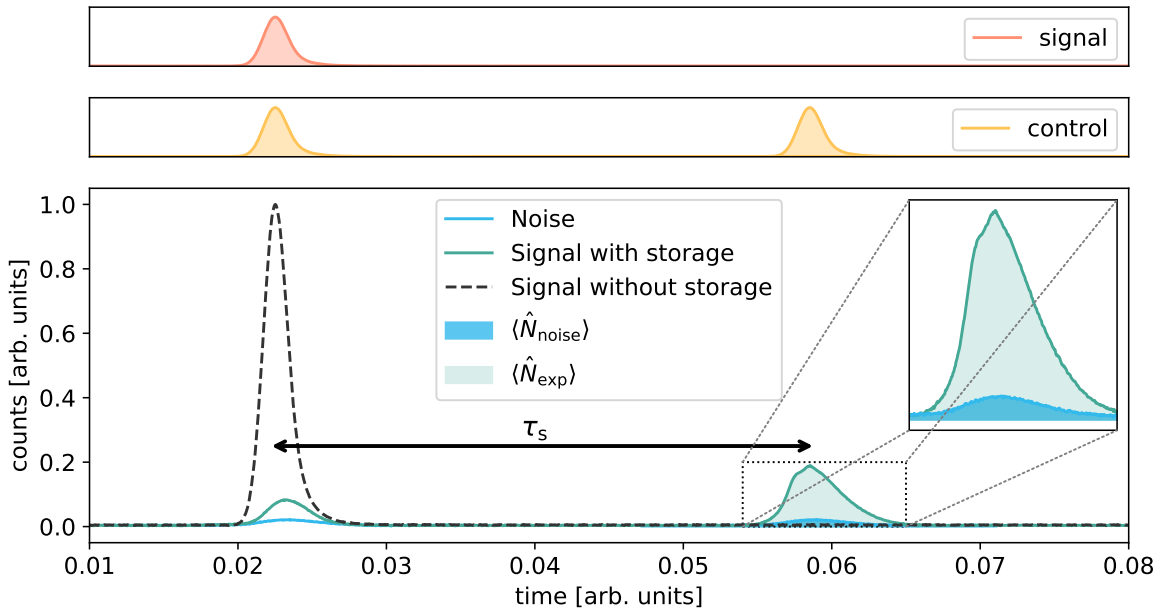

FIGURE 1 A typical photon arrival time histogram for an optically controlled memory experiment. The upper panels show the envelopes of the signal and the control field fed into the memory. The overlap of the control pulse with the signal pulse within the medium at time 0.22 maps the signal pulse to a collective spin-(orbital) wave. The experimental result (bottom panel) shows some leakage at this point in time from unstored light. After the storage time τ_s the control pulse is re-applied and the signal field is retrieved.

In this work we focus on photonic quantum memories in particular, i.e. memory devices that store information encoded in states of light. The most straight-forward way of storing light is in a fiber loop or Herriot cell. An incoming state of light is guided onto a long or, in the case of a fiber loop, closed light path that delays the transmission of the state. These implementations usually provide high fidelity and broadband operation but come with fixed read-in and read-out intervals [14]. This work concentrates on *optically controlled* ensemble-based memories. In these implementations a light field is used to exert control over the interaction between the light field to be stored and some atomic ensemble that serves as storage medium. During the read-in process the photonic state is mapped onto a coherent light-matter state, sometimes referred to as spinwave or (dark

state) polariton under an ideally unitary (time-reversible) transformation. This allows one to reverse the read-in process after the storage time τ_s and retrieve the initial photonic state. During the storage time the state undergoes some decoherence processes that heavily depend on the specific implementation. However, since both the read-in and read-out processes are (ideally) unitary the quantum coherence between the initial state and the retrieved state is conserved. An example of the storage and retrieval of a coherent state from an ensemble vapor memory can be seen in Figure 1. The signal pulse (red) is mapped onto the spinwave by applying the first control pulse (orange). After time τ_s, a second control pulse is sent into the atomic ensemble, and the state is retrieved from the memory (light blue).

There is a wide variety of different memory implementations with different properties that determine their suitability for application. In the next section, we describe the most important key characteristics on the basis of which ensemble quantum memories are compared.

2.1 | Characteristics and figures of merit

2.1.1 | Efficiency

The efficiency of a quantum memory describes the probability of retrieving a photon from the memory after a certain time, i.e. generally the memory efficiency is a function of the time between read-in and read-out. In some cases it is useful to describe the efficiency of the read-in and the read-out processes separately. The read-in efficiency η_{in} describes the probability of mapping a photon onto a coherent matter state when applying an optical control field. In the literature, it is sometimes referred to as storage efficiency. Respectively, the read-out efficiency η_{out} gives the probability of retrieving the photon field from the matter state at a later time. Combining the two, we define the internal efficiency $\eta_{\text{int}} = \eta_{\text{in}} \cdot \eta_{\text{out}}$ as the probability of successful read-in and read-out, not accounting for optical losses before or after the storage medium. Taking these into account, we define the end-to-end efficiency η_{e2e} which includes technical losses from the setup, $\eta_{\text{e2e}} = \eta_{\text{trans}} \cdot \eta_{\text{int}}$. A depiction of the different efficiency definitions can be found in Figure 2. Typical experiments achieve end-to-end efficiencies on the order of 1%-35%.

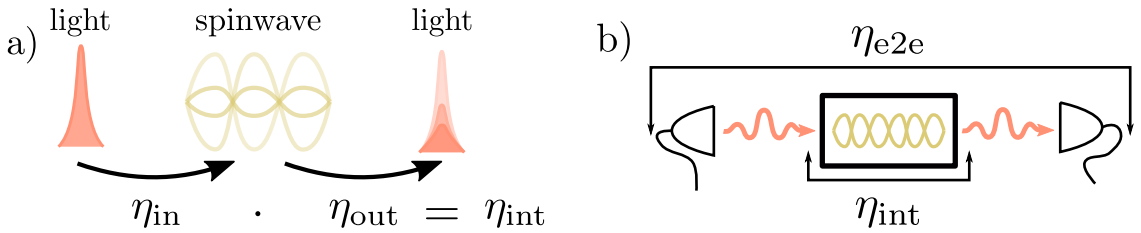

FIGURE 2 Internal and external efficiencies of a quantum memory. a) The incident light field gets stored in the spinwave with efficiency η_{in} and retrieved with efficiency η_{out} with a combined internal efficiency of η_{int}. b) The end-to-end efficiency η_{e2e} includes the optical transmission through the setup.

2.1.2 | Storage time

The time between read-in and read-out of a photonic state is generally referred to as storage time τ_s. During storage, the medium is subject to experiment specific decoherence processes which limit the storage time of the memory. In most cases homogeneous effects are dominant (i.e. all constituents of the storage medium undergo the same decoherence) and the internal efficiency exponentially decays with the storage time. Consequently, memory experiments report the 1/e storage time, also known as the memory lifetime, as a metric which can be used to compare different memory implementations. Typical storage times, depending on the memory protocol, range from nanoseconds to hundreds of microseconds.

Different ensemble based quantum memories use different memory protocols, that is, there is a different underlying physical process which controls the storage and retrieval process. A useful way to classify memories is to distinguish between memory implementations with fixed read-out intervals and *on-demand* read-out. Protocols that rely on the periodic rephasing of ensembles (e.g., atomic frequency combs - AFC) generally don't operate on demand; however, they may be modeled using the approach

below. It is left to the user to take care that read-out only occurs at the rephasing period. Another important metric that, together with the storage time, defines the memory's throughput is the memory downtime i.e. the time that is required to reinitialize the memory after a storage operation. The memory downtime is mostly limited by state preparation of the storage medium e.g. optical pumping.

2.1.3 | Operational wavelength and bandwidth

The operational wavelength of the memory depends on the atomic medium selected and its optical transitions. Most prominently, alkali metal vapors are used as storage media due to their strong and spectrally well-separated dipole transitions in the near infrared. The frequency of the input photon state has to be matched to the memory operation wavelength which is, within some detuning, determined by the chosen optical hyperfine transition. Detuning of the input signal from the optical transition can be beneficial in some memory implementations but heavily depends on the specific case.

The bandwidth of a memory $\Delta\nu_{\mathrm{mem}}$ determines the spectral width of an input photon $\Delta\nu_{\mathrm{ph}}$ that can be stored in the memory, see Figure 3. For Fourier-limited pulses the photon's spectral width is inversely proportional to its pulse width τ_{pulse}. Consequently, a short photon pulse to be stored requires a higher bandwidth of the memory. The ratio of memory storage time and shortest possible signal pulse length is called the fractional delay and gives an intuitive picture of the memory's ability to delay a pulse. The time-bandwidth product $B \sim \tau_s/\tau_{\mathrm{pulse}}$ of a memory is an equivalent measure which is most established in the literature. The product of the memory's time-bandwidth product and its end-to-end efficiency is regarded as the most important figure of merit of quantum memory implementations.

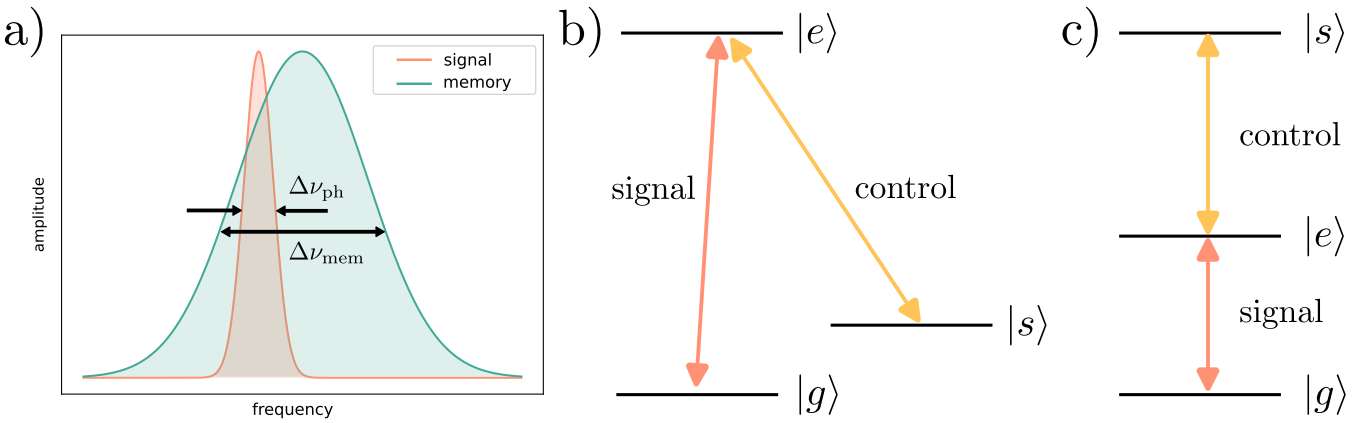

FIGURE 3 Bandwidth and memory type comparison. a) Spectral overlap of memory bandwidth and signal spectrum. For practical applications both signal wavelength and signal linewidth have to match the spectral properties of the memory. b) A memory in Λ-type configuration operates between ground- and storage states within one hyperfine manifold. c) Ladder-type memory configurations connect ground and storage state via full orbital transitions.

2.1.4 | Noise level

Memories with unit efficiency are rendered unusable if the number of noise photons in the retrieval mode exceeds the number of actually retrieved photons. Depending on the memory implementation, a plethora of physical mechanisms can influence the noise performance of a memory. Most prominently, optically controlled memories suffer from Four-wave mixing, Raman-noise and fluorescence. In principle, different noise levels can occur during read-in and read-out, which we account for in the simulation. The signal-to-noise ratio (SNR) is the most-used metric in the literature. It refers to the number of photons that are retrieved from the memory compared to the average number of detected noise photons during the retrieval:

$$\mathrm{SNR} = (\langle \hat{N}_{\mathrm{exp}} \rangle - \langle \hat{N}_{\mathrm{noise}} \rangle)/\langle \hat{N}_{\mathrm{noise}} \rangle \tag{1}$$

where $\langle \hat{N}_{\text{exp}} \rangle$ is the average number of total counts that are detected within the retrieval window, including the average number of noise photons $\langle \hat{N}_{\text{noise}} \rangle$. These parameters can be extracted from experimental data, such as the arrival time histogram shown in Figure 1. Another metric often used in the literature is the unconditional noise figure μ_1. It relates the SNR to the number of input photons $\langle N \rangle_{\text{in}}$ via:

$$\mu_1 = \frac{\langle N \rangle_{\text{noise}}}{\eta_{\text{int}}} = \frac{\langle N \rangle_{\text{in}}}{\text{SNR}}. \tag{2}$$

While the SNR is a figure that depends on the number of input photons the noise figure characterizes the number of noise photons alone. Importantly, we can use 2 to calculate the average number of noise photons from the μ_1 parameter which we will use in the simulation section (see Section 4). The μ_1 values in experiments are on the order of 10^{-2} to 10^{-6}.

2.1.5 | Single-photon operation

Interfacing existing memory implementations with true single-photon sources poses a significant challenge. The biggest problem lies in the bandwidth mismatch between single photons and memories. Quantum memories based on atomic ensembles typically exhibit bandwidths in the few MHz- to sub GHz-range. On the other hand, the most researched single-photon sources are based on solid-states (quantum dots, SPDC in bulk crystals etc.) and offer photon bandwidths from hundreds of MHz to hundreds of GHz. In addition to the bandwidth matching, the operational wavelengths of the single photon source and the memory have to be aligned. Considering the limited number of available dipole transitions in atomic ensembles, this is a highly non-trivial task. Moreover, for every type of photon source the read-in process has to be matched to the specific photon temporal envelope. Probabilistic photon sources come with the additional complexity of synchronizing the memory operation to the herald of a photon creation. Together with the numerous sources of background emission in the generation of single photons this places very stringent requirements on experimental implementations of true single photon storage. Previously, single photons from an SPDC sources have been coupled to a λ- type memory [15, 16, 17]. A ladder-type memory has been used to store and synchronize single photons from a room-temperature Four-Wave mixing source [18]. More recently, single photons from semiconductor quantum dots have been stored and retrieved from room-temperature ladder-type atomic vapor memories [19, 20].

2.1.6 | Fidelity

The fidelity of a quantum memory describes its ability to retrieve an unaltered quantum state from the memory. In its most general form it can be written as a comparison between two quantum states described by the density matrices $\hat{\rho}$ and $\hat{\sigma}$:

$$\mathcal{F} = \left(\text{tr} \sqrt{\sqrt{\hat{\rho}} \hat{\sigma} \sqrt{\hat{\rho}}} \right)^2 \tag{3}$$

. For pure states, the fidelity reduces to the overlap between the two states $\mathcal{F} = \left| \langle \psi_e | \psi_l \rangle \right|^2$. Even though the fidelity is arguably the most important memory performance metric, it is, paradoxically, rarely reported in the literature. The reason is that the measurement of $\mathcal{F}$ requires two full quantum tomography measurements of the in- and output states ρ and σ, which is notoriously difficult. In this regard, our digital twin model enables the inference of the fidelity performance from memory parameters that are much easier to access experimentally. The main effects that lowers the fidelity of a memory is the loss of photons and the generation of noise photons during read-out. In addition to that, the memory operation may imprint phase noise onto the state or distort the single photon wavepacket which generally results in an overall lower fidelity of a memory. The literature provides some results of memory experiments that measure the interferometric visibility of stored and un-stored light [21, 22] which can serve as an upper bound on the achievable memory fidelity. We include a simulation of state fidelities after a memory operation in the Appendix B.

2.1.7 | Operational simplicity and multi-mode capacity

Considering that a new infrastructure is required for the mass deployment of quantum memories, the operational simplicity of the technology is critical for long-range entanglement distribution. Compatibility with existing telecom fiber networks is desirable. Ideally, quantum memories can be micro-integrated or miniaturized [23, 24, 25] and operated without cryogenic

cooling. Low energy consumption and robustness against vibrations, temperature changes, radiation etc. is needed to allow for memory operation in space. Beyond these requirements, the ability to store more than one light mode in the same device (at the same time) is referred to as multi-mode capacity.[26, 27, 28]. It will be of critical importance in the scaling of quantum network infrastructures.

The atomic transitions that can be addressed during the storage process depend on selection rules and the light polarization. Therefore, ensemble-based memories are not polarization agnostic in general and each orthogonal polarization requires a separate memory mode. An important consequence of this fact is the requirement of at least two memories or memory modes to store a full polarization qubit [29]. Some of the memory implementations from the literature accept linear polarization and some only work with circular polarized light, which we have noted in the overview Table 1.

2.2 | Memory configurations and protocols

Quantum memories can operate in diverse regimes depending, for example, on their signal detuning from optical transitions, optical depth of the atomic ensemble or Rabi frequency. The different operating regimes result in different characteristics as discussed in the previous section. For detailed explanations of the different working regimes, we refer the reader to a review article on the topic [4]. In this section, we give a very brief explanation of the most fundamental differences between Λ-type and ladder-type configurations (see Figure 3), which aims to help to understand the performance differences between memories that can be seen in Table 2.

Fundamentally, the process of storage and retrieval relates a (collective) atomic ground state to a storage state via an intermediate state. In Λ-type configurations the storage state is within the same orbital level as the ground state only separated by the hyperfine splitting. The storage process results in a spin coherence between two states that are energetically separated by a few GHz (in the case of alkali ensembles). The wavevector difference $\Delta k = |k_s - k_c|$ between the signal and the control field that connect the ground state and the storage state determines the coherence length of the spinwave. Consequently, Λ-type memories with small wavevector differences show the longest reported storage time (e.g. [30, 31]). However, the small energy separation between signal and control fields comes with increased technical complexity due to spectral filtering and introduces noise channels to the system (e.g. Four-wave mixing, Raman noise). It can be seen from the overview table 2 that Λ-type memories have the lowest SNR values. On the other hand, ladder-type memories (sometimes referred to as Ξ-type) bring the advantage of almost noise-free operation due to the large energy separation between ground state and storage state. The drawback of this configuration lies in the short storage times (order of tens of nanoseconds) compared to Λ memories.

Within the broad categories of ladder and lambda memories, different operating parameters (signal detuning, control power ect.) result in different underlying physical processes mediating the storage process. These different operating regimes are called memory protocols, and determine the specific behavior of the memories. Off-resonant cascaded absorption (ORCA) and fast ladder memory (FLAME) are typical memory protocols for ladder memories, while Raman-electromagnetically induced transparency (EIT) and Raman-Autler-Townes splitting (ATS) usually refer to operating regimes in Lambda systems. We list the memory scheme and the protocol used in Table 1. For more details on the specific operation conditions and the memory protocols we refer to the review on broadband vapor memories [4].

Some characteristics such as operational simplicity, multi-mode capacity and single photon operation, are measures derived from demonstrated experimental implementation and are descriptive. Consequently they are not explicitly accounted for in the mathematical models we derive in the following section. The figures of merit, efficiency, storage time, operational wavelength and bandwidth, noise level, fidelity and polarization represent measurable parameters on the basis of which we can compare different memory implementations. In the next section we introduce the channel formalism and explain how the memories' figures of merit are implemented in the simulation.

3 | CHANNEL FORMALISM

To model different implementations of ensemble-based quantum memories, we define a general model for an ensemble vapor memory. First, we present the Hilbert space of the used formalism, before considering the memory process, and the experimental noise and losses. In Section 4 we explain the implementation details of our code and demonstrate some applications.

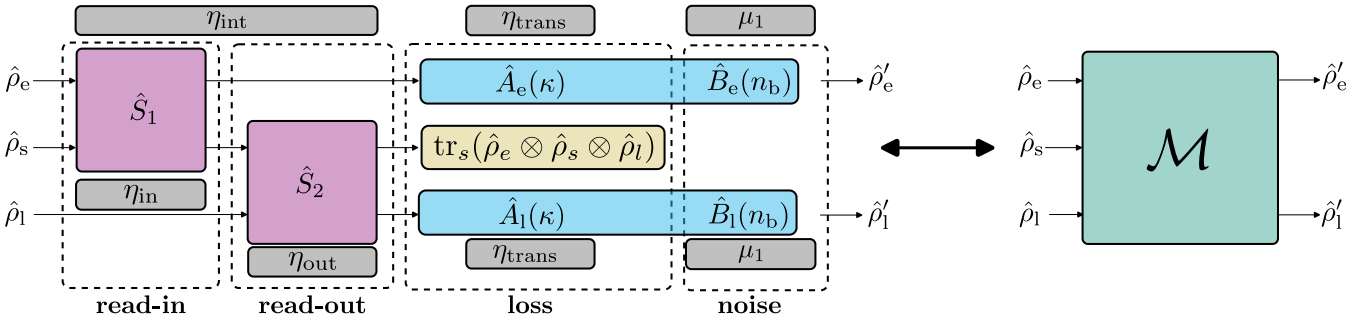

FIGURE 4 Depiction of the quantum memory operation in the quantum channel formalism. $\hat{\rho}_e, \hat{\rho}_l$ are the input states to the memory, corresponding to the states in the early and late time bin. $\hat{\rho}\prime_e, \hat{\rho}\prime_l$ are the early and late states after the memory operation. $\hat{\rho}_s$ is the state representing the spinwave, which is traced out after the memory operation. Every colored box corresponds to a set of Kraus operators with annotated parameters from memory experiments. The parameters in brackets correspond to the variables in the code. The memory box on the right serves as an abbreviated version for better readability.

3.1 | Hilbert space

We choose the Fock basis for the model and denote the path, polarization and time bin of the photons as mode indices. As such, the state $|n\rangle_{\{\text{X,p,t}\}}$ corresponds to n photons in path X, with polarization p, in the time bin t. Mode parameters which are not relevant to the system being modeled are then omitted i.e. if all photons in the system have the same polarization, we write the state as $|1\rangle_{\text{a,e}}$.

As a central tenet of memories is the delay of information from an earlier to a later time, the time-bin encoding of quantum information is common in the memory community. The Hilbert space acted on by the model is the joint space between two Hilbert spaces $\mathcal{H}_e \otimes \mathcal{H}_l$, where the input states of the memory are labeled with index e and the retrieved states in the late time bin with index l, respectively.

Memories are polarization-specific, and are often (although not exclusively) single path mode devices. Thus, we can simplify the notation down to the time-bin indices, i.e. $|1\rangle_e$. The joint state of say a single photon in the early time bin $|1\rangle_e$ and no photon in the late time bin $|0\rangle_l$ is then written $|1\rangle_e \otimes |0\rangle_l = |1_e, 0_l\rangle = |10\rangle$

In this work we present the operation of the memory using the channel formalism, that is states shall be written in density matrix form: $\hat{\rho}_e = \sum_n p_n \left(|\psi_n\rangle \langle\psi_n|\right)_e$, and the operators representing the memory are written in the Kraus form: $\sum_i K_i^\dagger K_i = 1$, where 1 is the identity.

A perfectly operating generalized memory stores an incoming photonic state $|n\rangle_e$ and perfectly returns that state at a later time.

$$\hat{S}\hat{\rho}_e\hat{S}^\dagger = \hat{\rho}_l$$

where $\rho_e = \rho_l$ and $\hat{S}$ one whole memory operation (read-in and read-out). However, physical memories are not perfect systems; the storage- and retrieval processes have limited efficiency, a single photon incident in the late time-bin may be stored, losses are present in the optical setup, and noise photons are present. Figure 4 depicts how each of these effects is represented in our model. In the following sections, we deal with each of these effects in turn in greater detail.

3.2 | Imperfect read-in and read-out

As mentioned in section 2.1.1 the memory process consists of two operations, the mapping of an incoming state to a spin wave (read-in), and the retrieval of the state from the atomic ensemble (read-out).

The read-in operator of an ensemble-based quantum memory, $\hat{S}_{\text{in}}$, transfers the incoming state $\hat{\rho}_e$ to a state $\hat{\rho}_s$, representing the internal state of the memory (spinwave). As the storage process is often imperfect, we model the storage operator as a beamsplitter with transmittivity, $t_{\text{in}} = 1 - \eta_{\text{in}}$, where η_{in}, is the read-in efficiency, defined as the fraction of photons successfully transferred to the spinwave. The leaked photons correspond to the photons remaining in the early time bin after the storage operation $\hat{S}_{in}$.

The read-out operator, $\hat{S}_{\text{out}}$, is a beamsplitter acting on the space $\mathcal{H}_s \otimes \mathcal{H}_l$, and controls the number of photons which are transferred from the spinwave to the late time-bin. The transmissivity of the $\hat{S}_{\text{out}}$ is $t_{\text{out}} = 1 - \eta_{\text{out}}$, where η_{out}, is the read-out

efficiency. Since the storage state ρ_s, is not actively monitored, it is treated as the environment and traced out after the read-in and read-out operations.

Formally, the read-in operation corresponds to the unitary operator

$$S_{\text{in}} = e^{\zeta(es^\dagger - e^\dagger s)}, \tag{4}$$

where κ is the coupling strength between the early time-bin mode and the memory storage mode. In practice this leads to a linear transformation of the mode operators

$$S_{in} : (e^\dagger s^\dagger) \rightarrow \begin{pmatrix} \sqrt{t_{\text{in}}} & \sqrt{r} \\ -\sqrt{r} & \sqrt{t_{\text{in}}} \end{pmatrix} * (e^\dagger s^\dagger), \tag{5}$$

where r is the beamsplitter reflectivity $r = 1 - t_{\text{in}}$ and $e^\dagger$ and $s^\dagger$ are the creation operators of the early and storage spaces. The coupling ζ relates to the beamsplitter parameters via $\cos(\zeta) = t$ and $\sin(\zeta) = r$. This form of the unitary acts on the creation and annihilation operators of the early and late states, however as the input states are in the full matrix representation of the Fock basis the beamsplitter must also be written in the same form:

$$\widehat{S}_{\text{in}} = \sum_{N=0}^{\infty} \sum_{n,m=0}^{N} S_{m,n}^{(N)} \left|N-m\right\rangle_e \left|m\right\rangle_s \left\langle N-n\right|_e \left\langle n\right|_s, \tag{6}$$

where the matrix element $S_{m,n}^{(N)}$ (dropping the in index for readability), is given by:

$$S_{m,n}^{(N)} = \frac{\sqrt{(N-n)n!}}{\sqrt{(N-m)m!}} \sqrt{t_{\text{in}}}^{N-2n} \left(\frac{\sqrt{r}}{\sqrt{t_{\text{in}}}}\right)^{m-n} P_n^{(m-n,N-n-m)}(t_{\text{in}} - r), \tag{7}$$

where $P_n^{(a,b)}(x)$ are the Jacobi polynomials. A derivation of this result can be found in the supplemental document. As it is often experimentally infeasible to determine the read-in and read-out efficiencies independently of one another, it is common practice not to report η_{in} and η_{out} individually, but rather the total internal efficiency $\eta_{\text{int}} = \eta_{\text{in}}\eta_{\text{out}}$. For the memories presented in this paper, we assume the read-in and read-out efficiency to be the same, $\eta_{\text{in}} = \eta_{\text{out}} = \sqrt{\eta_{\text{int}}}$, but the code easily allows for the treatment of unbalanced read-in and read-out efficiencies.

3.3 | Loss and Noise

To represent further losses in the channels and noise we treat the early and late states after the beamsplitters as inputs into a lossy thermal noise channel. To find a Kraus operator description, one decomposes the joint thermal noise channel into a pure loss channel of transmitivity $\tau = \kappa/G$ followed by a quantum limited amplifier with gain $G = 1 + (1-\kappa)\bar{n}_{\text{B}}$, where κ is the beamsplitter transmissivity and $\bar{n}_{\text{B}}$ is the mean thermal photon number of the noise channel [32]. This results in the following Kraus matrices for the pure loss channel A_l and the amplifier B_k.

$$\hat{A}_l = p_l \tau^{\frac{\hat{n}}{2}} \hat{a}^l, \tag{8}$$

$$\hat{B}_k = q_k \hat{a}^{\dagger k} G^{-\frac{\hat{n}}{2}}. \tag{9}$$

where $p_l = \sqrt{\frac{(1-\tau)^l}{l!}}$, $q_k = \sqrt{\frac{1}{k!}\frac{1}{G}\left(\frac{G-1}{G}\right)^k}$, $\hat{n}$ is the number operator and $a^{(\dagger)}$ are the creation (annihilation) operators. Thus, an input state ρ_0 then transforms according to $\rho = \sum_{k,l=0}^{\infty} \hat{B}_k \hat{A}_l \rho_0 \hat{A}_l^\dagger \hat{B}_k^\dagger$, where k, l are indicies to sum over the full fock space. In a truncated fock space, the sum does not go to infinity but to truncation n. In this form, the first the beam splitter operation representing loss $\hat{A}$, is applied before the gain operator. This is convenient as it lets us control the loss of ρ_0 with the transmissivity κ. This is analogous to losses through the experimental setup, after the storage operation and therefore the choice of $\kappa = \eta_{\text{trans}}$ is appropriate. By setting $\kappa = \eta_{\text{trans}}$ and applying the definition of μ_1 2 we can give an analytical formula for $\bar{n}_{\text{B}}$:

$$\bar{n}_B = \frac{\langle n \rangle_{\text{noise}}}{1 - \eta_{\text{trans}}} = \frac{\mu_1 \eta_{\text{int}}}{1 - \eta_{\text{trans}}}. \tag{10}$$

In treating the noise photons as a quantum limited amplifier, the computational complexity of the simulation increases. The truncation behavior of the simulation is presented in Appendix A. We set the truncation $n = 5$ for simulations with coherent

states and the truncation $n = 3$ for single photons unless otherwise stated. To simulate systems with higher input photon numbers, i.e. coherent states for $|\alpha\rangle$ where $|\alpha|^2 > 1$, the simulation truncation should be increased so that the output state converges.

4 | SIMULATION

The model presented above represents a number of simplifications of the underlying physics, which may affect the accuracy of memory performance simulations. In Section 4.1 we discuss both memory and input state initialization, the checks carried out to ensure compatibility between the two, as well as the limitations of these checks. In this section, further details of the operation of the memory channel query and an example query is shown. The use of the memory simulation in a Mach-Zehnder Interferometer experiment and in a quantum token protocol is presented in Section 5. An example implementation, can be found at [33]. To initiate the memory, the user must define several parameters of the memory itself and ensure the properties of the state which is to be stored match the properties of the memory. We first discuss the initialization of the memory, before considering the initialization of the input state.

4.1 | Memory Initialization

To simulate different atomic vapor memories, there are several properties which must be defined by the user upon initialization of the memory; these are, the memory type, the storage time, and the truncation of the internal memory state, and are further discussed below. An example initialization of the memory is given in **??** where a memory is initialized with a storage time of $\tau_s = 1\ \mu s$, and with a truncation bound of $n = 5$.

LISTING 1 The initalization of 'Lambda895' memory as demonstrated. The internal state of the memory is then initialized to be the vaccum state.

```
mem.set_param('memory_type', 'Lambda895')
mem.set_param('storage_time', 1e-6)
mem.set_param('memory_truncation', 5)
mem.send_params()
mem_state = mem.state_init()[0]
```

The first initialization parameter is the `memory type`, defining which memory should be used in the simulation. This is set using the `memory_type` parameter which takes a string as an argument. To access different memories, the user should provide the name of a memory class, which represents the different memory experiments. The names of the different classes (and thus memories) available can be found in Table 2. By setting the memory type using the command `mem.set_param("memory_type", 'Lambda895')` several characteristics of the memory, such as wavelength, polarization, bandwidth, lifetime are set automatically. This is important as the properties of the state that is to be stored, must match those of the memory. The parameters used in the memory modeling $t_{\text{in}}, t_{\text{out}}, \kappa$ and n_B are calculated from the η_{int} and η_{e2e}, as given in Table 2. We assume the read-in and read-out efficiency to be the same, such that $t_{in} = t_{out} = 1 - \sqrt{\eta_{\text{int}}}$. Alternatively, the users may specify their own parameters by setting the `memory_type` parameter to `Test`, and setting the operating parameters $t_{\text{in}}, t_{\text{out}}, \kappa_e, \kappa_l, n_{\text{B},e}, n_{\text{B},l}$ to custom values. The default values for the other parameters are $\lambda = 895$ nm, $\tau_s = 1\ \mu$s, $\Delta\omega = 500$ MHz, accepted polarization is either H, V and the $\tau_{\text{retrig}} = 1\ \mu$s. To determine the correct operating efficiency, the storage time must be initialized. This is the duration between the read-in and read-out of the memory, τ_s. As mentioned in Section 2.1, we consider only homogeneous decoherence effects and thus we model $\eta_{\text{int}}(t)$, the internal storage efficiency at time t, as an exponential $\eta_{\text{int}}(t) = \eta_{\text{int}}(0)\exp(-t/\tau)$. The $1/e$ storage times, τ for each memory can be found in Table 2. Setting the storage time has two effects, it sets the internal efficiency of the memory according to the exponential decay above, and sets the operation time of the system. The user must take caution that this exponential decay does indeed hold for the memory they would like to use. In the case where the transmisivities of the read-in and read-out beamsplitter t_{in}, t_{out} are user-defined, setting the storage time does not vary the beamsplitter transmissivity, so varying the storage time will have no effect. In this case, it is left to the user to account for the decay in storage efficiency. As the memory has its own internal state, the photon number at which the state is truncated must be set accordingly. This is done by setting the `truncation` parameter to an integer.

4.2 | State initialization

States that are to be stored in the memory, must have properties that match those of the memory. To ensure compatibility between the source and memory, several checks on the properties of incoming state are performed. Often, the relationship between the input photon properties and the effect on the memory operation is complex and has not been experimentally measured in all cases. As a result, we simplify the temporal and frequency behavior of the memory. A description of the source-memory compatibility checks and their limitations is provided below. The code snippet **??** shows the initialization of a state compatible with the memory initialized in **??**.

LISTING 2 The initalization of a state that is compatible with Lambda Cs D1 memory example above.

```
path_a_prop = StateProp(
        state_type="light",
        truncation=5,
        wavelength=894,
        polarization="V",
        uuid="a",
        bandwidth = 0.5e9
    )
```

The state to be stored in the memory has a specific wavelength and bandwidth, which should match that of the optimal operating conditions of the memory. Therefore, we apply a check that the wavelength of the state matches that of the memory within 1 nm, $\lambda_{\text{mem}} = \lambda_{\text{state}}$. Since the frequency dependence of noise and internal efficiency has not been reported for all memory experiments included in this work, proper consideration of the frequency compatibility of source and memory should be carried out independently, and was deemed beyond the scope of this work. To determine the eligibility of pairing a single photon source with a memory, further investigation into wavelength compatibility is required. Moreover, in the current implementation, photons with a bandwidth larger than that of the memory are rejected, $\Delta\nu_{\text{mem}} \geq \Delta\nu_{\text{state}}$. Experimentally, the memory functions as a frequency filter, storing photons whose frequency falls within the memory bandwidth window. Thus, the bandwidth behavior of the simulation does not fully represent the experimental behavior of the memory, but remains a topic for further extension of this simulation.

In this work, we reduce the time continuity of a memory experiment to discrete-time Fock states, representing early and late time bins. We explicitly do not consider the temporal shape and timing of the photons involved in the storage process. However, the photon envelope shape after storage in an ensemble-based vapor memory strongly depends on the temporal waveform shape of the control pulses. [6]. Furthermore, the read-in and read-out processes from the vapor memory may result in dispersion or phase distortion of the photon wavepacket. The extent of these effects is not fully understood, and remains a topic of ongoing research.

Finally, the polarization of the input state is compared to that of the memory. If they are in the same polarization orientation, the state is stored. We assume that the average noise photon μ_1 remains the same for both polarization orientations of the memory.

4.3 | Memory channel query

After initialization, the memory is queried, and the Kraus operators representing the read-in and read-out operations are returned and applied to the corresponding states. An example of a read-in operation is shown in code snippet **??**.

LISTING
3 An example query of the memory, returning the Kraus operators for the read-in operation. Here the type of operation ('storage', 'retrieval) is chosen by setting 'op_type': 'storage'. The read-in operation is then applied to the input state, and the internal state of the memory

```
response, operators = mem1.channel_query(
        whole_state, {"input": state_path_a_h_prop.uuid, 'op_type': 'storage'}
    )

whole_state.apply_kraus_operators(operators, whole_state.get_all_props(response["kraus_state_indices"]))
```

To represent the different operation timescales of the memory, a memory query returns two different timings: the operation time and the re-triggering rate. The operation time is the storage time specified by the user in initialization. The re-triggering time is the time until a memory experiment can be repeated. Experimentally, this is the operation time plus the time taken for

other experimental processes, such as pumping, cooling, and trigger delays. If no pumping is present in the experiment, the re-triggering rate is assumed to be the operation time. The operation and re-triggering times are given in Table 1. When a photon is stored in the memory, that is when the channel is queried with op_type = storage, re-trigger is set to false. Upon a channel query with the op_type = retrieval, the re-trigger is set to true. We assume that the passage of a second single photon through the memory during the storage time does not result in further decoherence of the memory state.

5 | EXAMPLES

In the following section, we present example applications of digital twins, specifically the simulation of a Mach-Zehnder interferometer with a memory element in one of its arms, and the storage of quantum tokens.

5.1 | Visibility and fidelity simulations for memories

To demonstrate the compatibility of the memory simulation with both single photons and coherent states, we measure the interference fringes observed when states are sent into a Mach-Zehnder Interferometer (MZI) with a phase element in one arm, and a memory element in the other (as shown in Figure 5a). The beamsplitters are assumed to have 50% transmission/reflection and the memory implementation in [34] has been chosen as an example, due to its high noise, $\mu_1 = 0.07$. The path interference for a single photon input state and coherent state input with $\alpha = 1.5$ is shown in Figure 5b. We derive analytical solutions for the average photon number in mode A, for single photons and coherent states, which are depicted as full and dashed lines respectively (see supplementary information). As one can see, we observe excellent agreement between simulation and theory. To examine the behavior of the system without interference between the two modes, we remove the second beamsplitter. The memory exhibits a zero-time end-to-end efficiency of $\eta_{\text{e2e}}(0) = 0.13$ which reflects in the lowered transmission through path A in the absence of the second beamsplitter (plotted in yellow). The visibility in an MZI configuration is an important measure for the indistinguishability of quantum states which has to be preserved by quantum memories in practical applications. Indeed for single photons, fringe visibility is an upper bound on the two photon interference visibility value of photons stored in a quantum memory. We calculate the visibility for a mode, given as:

$$v = \frac{\langle \hat{n} \rangle_{\max} - \langle \hat{n} \rangle_{\min}}{\langle \hat{n} \rangle_{\max} + \langle \hat{n} \rangle_{\min}}.$$

Here $\langle \hat{n} \rangle_{\max}$ ($\langle \hat{n} \rangle_{\min}$) are the maximum (minimum) average number of photons measured in a single arm. We see in Figure 5 b) that the presence of noise from the memory lowers the visibility of the interference. In Figure 6 we compare the fringe

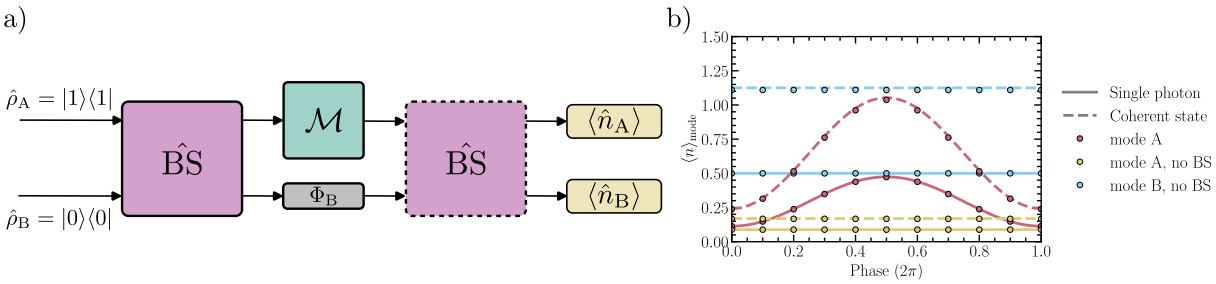

FIGURE 5 a) Quantum channel diagram for a Mach-Zehnder Interferometer (MZI). A single photon is sent into path mode A and the average photon numbers in mode A and mode B are measured. b) The average photon number $\langle \hat{n} \rangle$ in mode A of the MZI is shown in red, for a single photon input (solid line) and for a coherent state input $\alpha = 1.5$ (dashed line). The blue and yellow curves show the average photon number in modes A and B, respectively, with the second beamsplitter removed. The data points represent simulated values, while the curves correspond to theoretical predictions from analytical solutions (see MZI section of the supplementary document). An excellent agreement between the analytical predictions and simulated results is observed. The truncation for the coherent state simulation is $n = 7$.

visibility in the MZI configuration for some of the most recent atomic vapor memories (see Table 2) assuming single-photon input. We find that memories with both high efficiency and lowest noise figure exhibit the highest fringe visibility. As expected, the visibility for all memories decreases exponentially with time according to their decrease in efficiency.

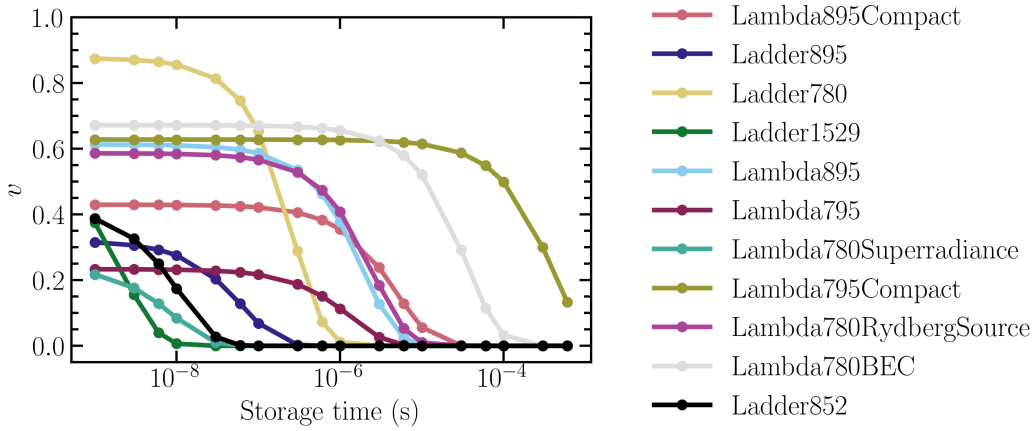

FIGURE 6 Visibility of the single photon MZI interference fringes after storage in a memory, as a function of storage time.

5.2 | Quantum token protocol

To demonstrate an application of the memory simulation, we simulate a quantum token protocol, based on the experimental implementation described in [35]. Quantum token protocols are used to safely encode classical information in qubits using either one of two basis sets x and z, i.e. $x = \{|0\rangle, |1\rangle\}, z = \{|+\rangle, |-\rangle\}$. Due to the no-cloning theorem, only a party knowing the basis used to encode the classical bit can unambiguously recover the encoded information. Imperfections in such protocols are described in terms of correctness parameters c_{ij}, which is the probability of recovering the correct classical bit that was encoded in basis $i = x, z$ when measuring in basis $j = x, z$. Here we focus on the composite correctness parameter $c = \frac{1}{2}(c_{xx} + c_{zz}$, which yields $c = 1$ for a perfect quantum token experiment and $c = 1/2$ for a token experiment exhibiting random behaviour.

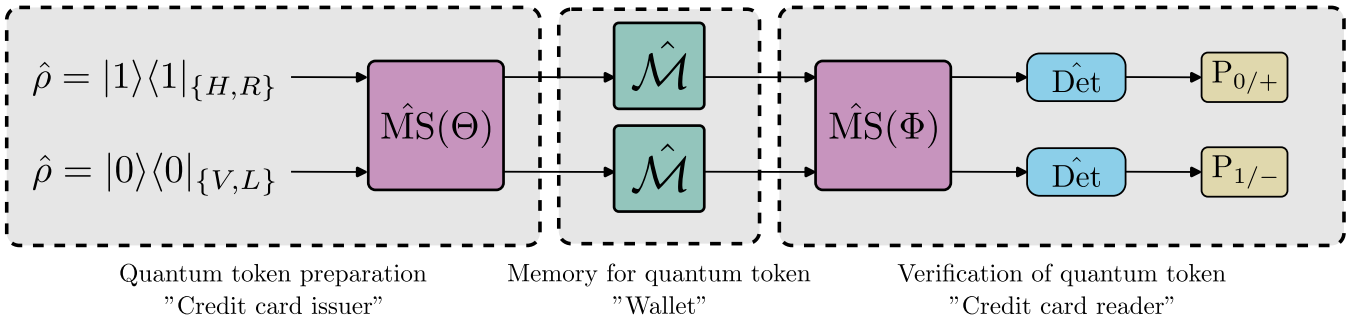

FIGURE 7 Quantum channel description of a quantum token protocol. A polarization encoded quantum token is prepared (either in H and V or L and R) and stored in two memories, one for each orthogonal polarization. After the retrieval from the memory the token is decoded and the click probability is measured on noisy orthogonal detectors.

In the experimental implementation demonstrated in [35] the computational basis states are mapped onto polarization states of the photons. Given the memories accept a single polarization orientation, the basis must match that of the memory. Thus for memories which accept H/V polarization orientations we map $|0\rangle = |H\rangle, |1\rangle = |V\rangle$, and $|+\rangle = |D\rangle, |-\rangle = |A\rangle$. For the R/L

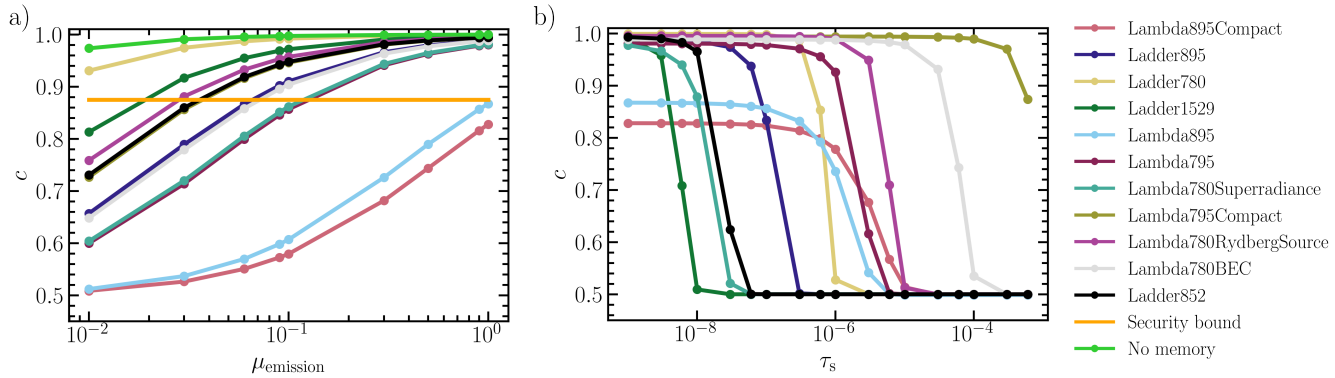

FIGURE 8 a) Simulated correctness values for different memories used in the protocol, with $\tau_s = 0$. The expected correctness of the system without memory is shown in green. b) The variation of the correctness of a memory token as a function of storage time for $\mu_{\text{emission}} = 1$. 'Lambda795Compact' has a lifetime of 180 μs, enabling high token correctness for long storage times.

polarization basis $|0\rangle = |R\rangle, |1\rangle = |L\rangle$, and $|+\rangle = |H\rangle, |-\rangle = |V\rangle$. In the model, polarization is given as labeled Fock states, with orthogonal polarizations having two different states, e.g $|+\rangle = \frac{1}{\sqrt{2}}(|1\rangle_H + |1\rangle)_V$. To prepare a token in a given state, a horizontal Fock state, and the vacuum vertical state are sent to the tunable mode selector ($\hat{MS}$). The mode selector acts as a beam splitter with the matrix representation:

$$\hat{MS}(\theta) = \begin{pmatrix} \cos 2\theta & \sin 2\theta \\ \sin 2\theta & -\cos 2\theta \end{pmatrix}. \tag{11}$$

By setting the $\theta = \pi/2,\ 3\pi/4, 3\pi/8, 5\pi/8$ the incoming $|1\rangle_{\{H,R\}} + |0\rangle_{\{V,L\}}$, returns the states $|0\rangle, |1\rangle, |-\rangle, |+\rangle$, respectively. In the H/V state encoding basis, the mode selector can be considered as the combined perfect action of a $\lambda/2$ waveplate and a polarizing beamsplitter. After storage in two memories that accept the orthogonal polarization directions, the states are then read out of the memories and sent to a second mode selector, which sets the measurement basis. Setting $\Phi = \pi/2$ ($5\pi/8$), sets the measurement basis to the $z(x)$ basis, respectively. We model detector loss and dark counts using the Kraus operators presented in 3.3, where $\kappa = 0.25$ and $n_b = \frac{7\times10^{-5}}{1-\kappa}$, corresponding to the values given in [35].

We consider the calculation of c_{zz} from the simulation in Figure 7. The correctness of the measurement of photons prepared in the z basis, is an average of measuring the $|0\rangle$ and $|1\rangle$ states correctly, $c_{zz} = \frac{1}{2}(c_0 + c_1)$. The preparation of perfectly polarized photons in state $|0\rangle$ and measurement in the z basis, will result in a click in the detector in path mode 0/+, measuring '0'. Likewise, the preparation of a photon in state $|1\rangle$ will result in a click in the detector in path 1/–, measuring the state to be '1'. Sending in the state $|0\rangle$ and measuring a click on detector 1/–, corresponds to a wrong result, and thus reduces the correctness. The correctness of measuring $|0\rangle$, given a measurement in the z basis is, $c_0 = \frac{P_{\text{click only 0/+}}}{P_{\text{click either}}}$, where $P_{\text{click only 0/+}}$ is the probability of getting a click only in the detector in path measuring the states $|0\rangle, |+\rangle$ and $P_{\text{click either}}$ is the probability of getting at least one click in either arm. Thus if $P_{0/+}$ is the probability of measuring a photon as 0/+, and $P_{1/-}$ the probability of measuring a photon as being in state 1/–, then $c_0 = \frac{P_{0/+}(1-P_{1/-})}{1-(1-P_{0/+})(1-P_{1/-})}$ and similarly the correctness of measuring $|1\rangle$, $c_1 = \frac{P_{1/-}(1-P_{0/+})}{1-(1-P_{1/-})(1-P_{0/+})}$. The probability of measuring at least one photon, is given by $P_{0/+} = \sum_{i=1}^{N}\sum_{j=0}^{N}\langle i,j|\,\rho\,|i,j\rangle$, $P_{1/-} = \sum_{i=1}^{N}\sum_{j=0}^{N}\langle j,i|\,\rho\,|j,i\rangle$, where the state $|i,j\rangle = |i\rangle_{\{H,R\}}\,|j\rangle_{\{V,L\}}$. To measure $c_{xx} = \frac{1}{2}(c_+ + c_-)$, one repeats the simulation, with input states corresponding to $|+\rangle, |-\rangle$, and measurement in the x basis.

Figure 8 a) shows the correctness of quantum tokens stored in different memories, with respect to the single photon emission probability, μ_{emission}. For perfect on-demand photons, $\mu_{\text{emission}} = 1$, most memory implementations achieve a correctness above the single photon correctness threshold to ensure the security of the quantum token protocol, $c > 7/8$ [35] (shown in orange). However, achieving an almost perfectly efficient single photon source with high purity is experimentally challenging. A clear factor influencing the correctness for low photon emission probabilities is the signal to noise ratio. Memories based on the ORCA/FLAME protocol with SNR on the order of $\sim 10^3$, result in the highest correctness. The two memories with the highest μ_1 do not reach the security threshold, even for a perfect single-photon emission probability. Importantly, these results give upper bounds for the correctness, as $\tau_s = 0$. To simulate the correctness of different memories at varying storage times, we set $\mu_{\text{emission}} = 1$, and scan τ_s between 1 ns to 600 us. Figure 8 b) shows the storage time dependence of the correctness parameter of each memory implementation.

6 | CONCLUSION

We develop a quantum channel description of ensemble based atomic vapor memories and provide model parameters for state-of-the-art quantum memory experiments. We use our model to estimate upper bounds for the visibility of a HOM-type measurement for single photons stored in a memory and observe excellent agreement between theory and simulations. Furthermore, we use the digital twin of the memories in assessing the security of a quantum token protocol. We compare the performance of different memory implementations from the literature. To further extend the applicability of the digital twins within quantum network simulations, proper consideration of frequency and temporal effects is needed. Matching of the memory bandwidth and photon temporal wavepacket as well as the inclusion of dispersive effects is subject of future work. The model presented allows for easy extension to include and compare other optically controlled memories such as solid-state memories. The presented digital twins are embedded in an easy-to-use simulation framework which allows for straightforward estimates of memory performances in multi-device quantum networks and are a step toward full end-to-end experimental simulation of quantum optics experiments.

ACKNOWLEDGMENTS

We would like to thank Leon Messner for humorously insightful discussions. The authors acknowledge financial support from DFG project 448532670 and BMFTR through project 16KIS1717K.

DATA AVAILABILITY

The data is available from the authors upon reasonable request.

CONFLICT OF INTEREST

The authors declare no potential conflict of interests.

SUPPORTING INFORMATION

Additional supporting information may be found in the online version of the article at the publisher's website.

REFERENCES

1. H. J. Kimble, Nature **453**(7198), 1023 (2008), Publisher: Nature Publishing Group.
2. L.-M. Duan, M. D. Lukin, J. I. Cirac, P. Zoller, Nature **414**(6862), 413 (2001), Publisher: Nature Publishing Group.
3. Alexander I. Lvovsky, Barry C. Sanders, Wolfgang Tittel, Nature Photonics **3**(12), 706 (2009), Publisher: Nature Publishing Group.
4. Kai Shinbrough, Donny R. Pearson Jr, Bin Fang, Elizabeth A. Goldschmidt, Virginia O. Lorenz, *Broadband Quantum Memory in Atomic Ensembles* (2023), arXiv:2301.08772 [quant-ph]. http://arxiv.org/abs/2301.08772.
5. Alexey V. Gorshkov, Axel André, Michael Fleischhauer, Anders S. Sørensen, Mikhail D. Lukin, Physical Review Letters **98**(12), 123601 (2007).
6. Irina Novikova, Alexey V. Gorshkov, David F. Phillips, Anders S. Sørensen, Mikhail D. Lukin, Ronald L. Walsworth, Physical Review Letters **98**(24), 243602 (2007).
7. Nathan Killoran, Josh Izaac, Nicolás Quesada, Ville Bergholm, Matthew Amy, Christian Weedbrook, Quantum **3**, 129 (2019), arXiv:1804.03159 [quant-ph].
8. Nicolas Heurtel, Andreas Fyrillas, Grégoire de Gliniasty, Raphaël Le Bihan, Sébastien Malherbe, Marceau Pailhas, Eric Bertasi, Boris Bourdoncle, Pierre-Emmanuel Emeriau, Rawad Mezher, Luka Music, Nadia Belabas, Benoît Valiron, Pascale Senellart, Shane Mansfield, Jean Senellart, Quantum **7**, 931 (2023), Publisher: Verein zur Förderung des Open Access Publizierens in den Quantenwissenschaften.
9. Zoltán Kolarovszki, Tomasz Rybotycki, Péter Rakyta, Ágoston Kaposi, Boldizsár Poór, Szabolcs Jóczik, Dániel T. R. Nagy, Henrik Varga, Kareem H. El-Safty, Gregory Morse, Michał Oszmaniec, Tamás Kozsik, Zoltán Zimborás, *Piquasso: A Photonic Quantum Computer Simulation Software Platform* (2025), arXiv:2403.04006 [quant-ph]. http://arxiv.org/abs/2403.04006.
10. Neill Lambert, Eric Giguère, Paul Menczel, Boxi Li, Patrick Hopf, Gerardo Suárez, Marc Gali, Jake Lishman, Rushiraj Gadhvi, Rochisha Agarwal, Asier Galicia, Nathan Shammah, Paul Nation, J. R. Johansson, Shahnawaz Ahmed, Simon Cross, Alexander Pitchford, Franco Nori, *QuTiP 5: The Quantum Toolbox in Python* (2024), arXiv:2412.04705 [quant-ph]. http://arxiv.org/abs/2412.04705.
11. Ali Javadi-Abhari, Matthew Treinish, Kevin Krsulich, Christopher J. Wood, Jake Lishman, Julien Gacon, Simon Martiel, Paul D. Nation, Lev S. Bishop, Andrew W. Cross, Blake R. Johnson, Jay M. Gambetta, *Quantum computing with Qiskit* (2024), arXiv:2405.08810 [quant-ph]. http://arxiv.org/abs/2405.08810.
12. Javier Osca, Jiri Vala, SoftwareX **25**, 101603 (2024), arXiv:2307.06965 [quant-ph].
13. W. K. Wootters, W. H. Zurek, Nature **299**(5886), 802 (1982), Publisher: Nature Publishing Group.
14. Kim Fook Lee, Gamze Gül, Zhao Jim, Prem Kumar, New Journal of Physics **26**(8), 083011 (2024), Publisher: IOP Publishing.
15. Gianni Buser, Roberto Mottola, Björn Cotting, Janik Wolters, Philipp Treutlein, PRX Quantum **3**(2), 020349 (2022), Publisher: American Physical Society.
16. Pin-Ju Tsai, Ya-Fen Hsiao, Ying-Cheng Chen, Physical Review Research **2**(3), 033155 (2020).
17. P S Michelberger, T F M Champion, M R Sprague, K T Kaczmarek, M Barbieri, X M Jin, D G England, W S Kolthammer, D J Saunders, J Nunn, I A Walmsley, New Journal of Physics **17**(4), 043006 (2015).
18. Omri Davidson, Ohad Yogev, Eilon Poem, Ofer Firstenberg, Physical Review Letters **131**(3), 033601 (2023), Publisher: American Physical Society.
19. Sarah E. Thomas, Lukas Wagner, Raphael Joos, Robert Sittig, Cornelius Nawrath, Paul Burdekin, Ilse Maillette de Buy Wenniger, Mikhael J. Rasiah, Tobias Huber-Loyola, Steven Sagona-Stophel, Sven Höfling, Michael Jetter, Peter Michler, Ian A. Walmsley, Simone L. Portalupi, Patrick M. Ledingham, Science Advances **10**(15), eadi7346 (2024), Publisher: American Association for the Advancement of Science.

20. Benjamin Maaß, Avijit Barua, Norman Vincenz Ewald, Elizabeth Robertson, Kartik Gaur, Suk In Park, Sven Rodt, Jin-Dong Song, Stephan Reitzenstein, Janik Wolters, *On-demand storage and retrieval of single photons from a semiconductor quantum dot in a room-temperature atomic vapor memory* (2025), arXiv:2501.15663 [quant-ph]. http://arxiv.org/abs/2501.15663.
21. K. F. Reim, J. Nunn, V. O. Lorenz, B. J. Sussman, K. C. Lee, N. K. Langford, D. Jaksch, I. A. Walmsley, Nature Photonics **4**(4), 218 (2010), Publisher: Nature Publishing Group.
22. Erhan Saglamyurek, Taras Hrushevskyi, Anindya Rastogi, Khabat Heshami, Lindsay J. LeBlanc, Nature Photonics **12**(12), 774 (2018), Publisher: Nature Publishing Group.
23. Roberto Mottola, Gianni Buser, Philipp Treutlein, Physical Review Letters **131**(26), 260801 (2023), Publisher: American Physical Society.
24. Martin Jutisz, Alexander Erl, Janik Wolters, Mustafa Gündoğan, Markus Krutzik, Physical Review Applied **23**(2), 024045 (2025), Publisher: American Physical Society.
25. Yu-Ping Liu, Zhong-Wen Ou, Tian-Xiang Zhu, Ming-Xu Su, Chao Liu, Yong-Jian Han, Zong-Quan Zhou, Chuan-Feng Li, Guang-Can Guo, Science Advances **11**(13), eadu5264 (2025), Publisher: American Association for the Advancement of Science.
26. C. Li, S. Zhang, Y.-K. Wu, N. Jiang, Y.-F. Pu, L.-M. Duan, PRX Quantum **2**(4), 040307 (2021).
27. Leon Messner, Elizabeth Robertson, Luisa Esguerra, Kathy Lüdge, Janik Wolters, Optics Express **31**(6), 10150 (2023), Publisher: Optica Publishing Group.
28. Sheng Zhang, Jixuan Shi, Zhaibin Cui, Ye Wang, Yukai Wu, Luming Duan, Yunfei Pu, Physical Review X **14**(2), 021018 (2024), Publisher: American Physical Society.
29. Mehdi Namazi, Connor Kupchak, Bertus Jordaan, Reihaneh Shahrokhshahi, Eden Figueroa, Physical Review Applied **8**(3), 034023 (2017), Publisher: American Physical Society.
30. Or Katz, Ofer Firstenberg, Nature Communications **9**(1), 2074 (2018), Publisher: Nature Publishing Group.
31. Yang Wang, Alexander N. Craddock, Rourke Sekelsky, Mael Flament, Mehdi Namazi, Physical Review Applied **18**(4), 044058 (2022), Publisher: American Physical Society.
32. Christos N. Gagatsos, Boulat A. Bash, Saikat Guha, Animesh Datta, Physical Review A **96**(6), 062306 (2017), arXiv:1701.05518 [quant-ph].
33. Elizabeth Robertson . https://github.com/erlizzard/quantum-memory-digital-twin.git.
34. Luisa Esguerra, Leon Meßner, Elizabeth Robertson, Norman Vincenz Ewald, Mustafa Gündoğan, Janik Wolters, Physical Review A **107**(4), 042607 (2023), Publisher: American Physical Society.
35. Mathieu Bozzio, Adeline Orieux, Luis Trigo Vidarte, Isabelle Zaquine, Iordanis Kerenidis, Eleni Diamanti, npj Quantum Information **4**(1), 1 (2018), Publisher: Nature Publishing Group.
36. Benjamin Maaß, Norman Vincenz Ewald, Avijit Barua, Stephan Reitzenstein, Janik Wolters, Physical Review Applied **22**(4), 044050 (2024), Publisher: American Physical Society.
37. Omri Davidson, Ohad Yogev, Eilon Poem, Ofer Firstenberg, Communications Physics **6**(1), 1 (2023), Publisher: Nature Publishing Group.
38. S.E. Thomas, S. Sagona-Stophel, Z. Schofield, I.A. Walmsley, P.M. Ledingham, Physical Review Applied **19**(3), L031005 (2023), Publisher: American Physical Society.
39. Anindya Rastogi, Erhan Saglamyurek, Taras Hrushevskyi, Lindsay J. LeBlanc, Physical Review Letters **129**(12), 120502 (2022), Publisher: American Physical Society.
40. L. Heller, J. Lowinski, K. Theophilo, A. Padrón-Brito, H. de Riedmatten, Physical Review Applied **18**(2), 024036 (2022), Publisher: American Physical Society.
41. Erhan Saglamyurek, Taras Hrushevskyi, Anindya Rastogi, Logan W Cooke, Benjamin D Smith, Lindsay J LeBlanc, New Journal of Physics **23**(4), 043028 (2021), Publisher: IOP Publishing.
42. K. T. Kaczmarek, P. M. Ledingham, B. Brecht, S. E. Thomas, G. S. Thekkadath, O. Lazo-Arjona, J. H. D. Munns, E. Poem, A. Feizpour, D. J. Saunders, J. Nunn, I. A. Walmsley, Physical Review A **97**(4), 042316 (2018), Publisher: American Physical Society.
43. Yan-Cheng Wei, Bo-Han Wu, Ya-Fen Hsiao, Pin-Ju Tsai, Ying-Cheng Chen, Physical Review A **102**(6), 063720 (2020), Publisher: American Physical Society.
44. Pierre Vernaz-Gris, Kun Huang, Mingtao Cao, Alexandra S. Sheremet, Julien Laurat, Nature Communications **9**(1), 363 (2018), Publisher: Nature Publishing Group.

□

APPENDIX

A TRUNCATION

We analyze the truncation of our presented memory simulation by varying the truncation of a memory experiment for the memory with the lowest signal-to-noise ratio (highest μ_1). We simulate a memory experiment with the input state $\hat{\rho} = |1\rangle\langle 1|$ and $\hat{\rho} = |\alpha\rangle\langle\alpha|$ where $\alpha = 1$, respectively. We measure the average photon number of the late time-bin, and observe the convergence with increasing truncation. Figure A1 shows the convergence of the expected photon number at a truncation of 5 for coherent states, and 3 for single photons. To simulate coherent states with $\alpha > 1$ a higher truncation will be required. This quickly scales the size of the state space needed to simulate the memory, making simulation of coherent states impractical for $\alpha \gtrapprox 1$.

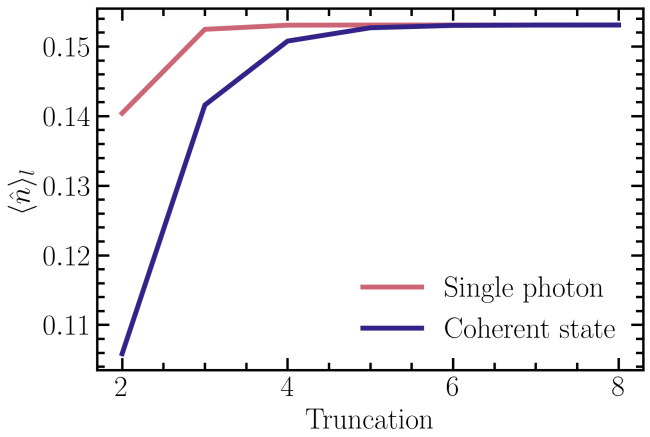

FIGURE A1 Convergence of the average photon number after storage in a 'Lambda895' memory.

B FIDELITY SIMULATIONS FOR TEST MEMORIES

When assessing the performance of a quantum memory, a central question is: To what extent is the quantum state input to the memory preserved after retrieval? A natural approach is to evaluate the state overlap between the retrieved state $\hat{\sigma}$, and the input state $\hat{\rho}$, defined as:

$$\mathcal{F}(\hat{\rho}, \hat{\sigma}) = \left(\mathrm{tr}\sqrt{\sqrt{\hat{\rho}}\hat{\sigma}\sqrt{\hat{\rho}}} \right)^2 . \tag{B1}$$

By construction $\mathcal{F} = 1$ if $\hat{\sigma} = \hat{\rho}$. A benefit of our simulation is that we can easily access both $\hat{\sigma}$ and $\hat{\rho}$, which in experiment typically would require two full state tomography measurements. However, we show below that care must be taken when interpreting this quantity, especially for different input states and in the presence of loss and noise.

The simulated fidelity values for two types of input states — single photons and coherent states with $\alpha = 1$ —are illustrated in Figure B2a. Here we simulate an ideal memory with perfect transmission efficiency ($\eta_{\mathrm{trans}} = 1$) and no background noise ($n_{\mathrm{B}} = 0$). For single photons, the fidelity increases linearly with the internal efficiency of the memory, reflecting the improving preservation of the input state. In contrast, the fidelity of coherent states does not vanish even as the internal efficiency η_{int} approaches zero. This is due to the non-zero vacuum component of coherent states — when the output is vacuum, the overlap with the original state still yields a fidelity of $\mathcal{F} = e^{-|\alpha|^2}$.

By measuring fidelity and signal-to-noise ratio (SNR) with increasing noise photon number, we further observe the difference in fidelity between coherent states and single photon inputs, as seen in Figure B2 b). While SNR decreases with added noise – as expected -— the fidelity of both states saturates to a non-zero value. Moreover, depending on the input state, the measured fidelity varies between input coherent state, and single photon - for the same SNR. Additionally, for the same SNR, the measured fidelity can differ depending on whether the input state is a single photon or a coherent state. This behavior underscores the

importance of comparing memory fidelities only when the same input state is used, as differences in input can lead to misleading conclusions about performance.

Fidelity measurements for a coherent state $\alpha = 1$ stored in various quantum memories are presented in Figure B3. For high state fidelity after the memory, the improvement of the overall memory end-to-end efficiency is key.

When assessing fidelity for single-photon inputs, it is important to recognize that the state $\hat{\rho} = |1\rangle\langle 1|$ has no phase coherence. As a result, the addition of incoherent noise photons can increase the fidelity -— not due to improved memory performance, but because the input state more closely resembles the incoherent noise. This effect should not be interpreted as an enhancement of memory quality.

In summary, fidelity remains a valuable figure of merit which we can easily measure in our model, however its interpretation requires careful consideration of the state input into the memory. Specifically, fidelity comparisons should only be made between memories tested with the same input states, particularly in realistic, noisy, or lossy conditions.

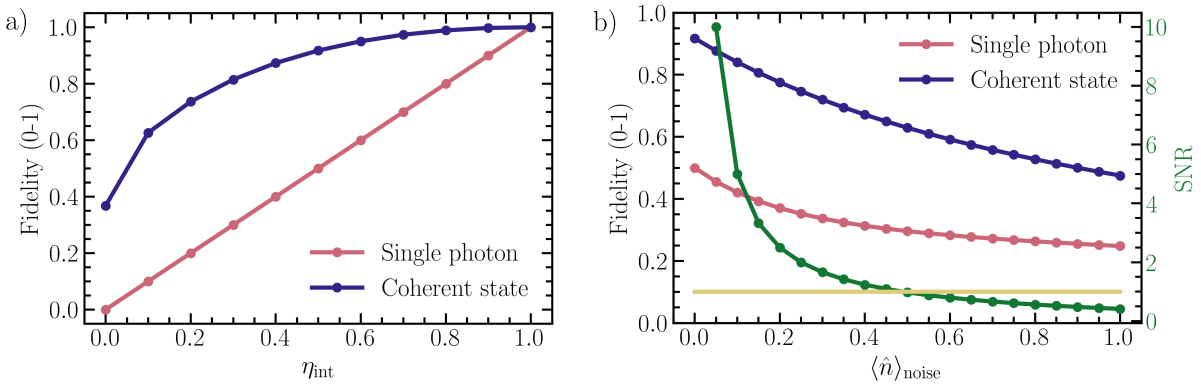

FIGURE B2 a) Variation of the fidelity of photons out of a memory, with no noise, and varying internal efficiency. b) Fidelity of a memory with perfect internal efficiency, loss of 0.5, and varying noise photons. The signal-to-noise ratio is plotted in green, and the bound SNR = 1 is shown in yellow.

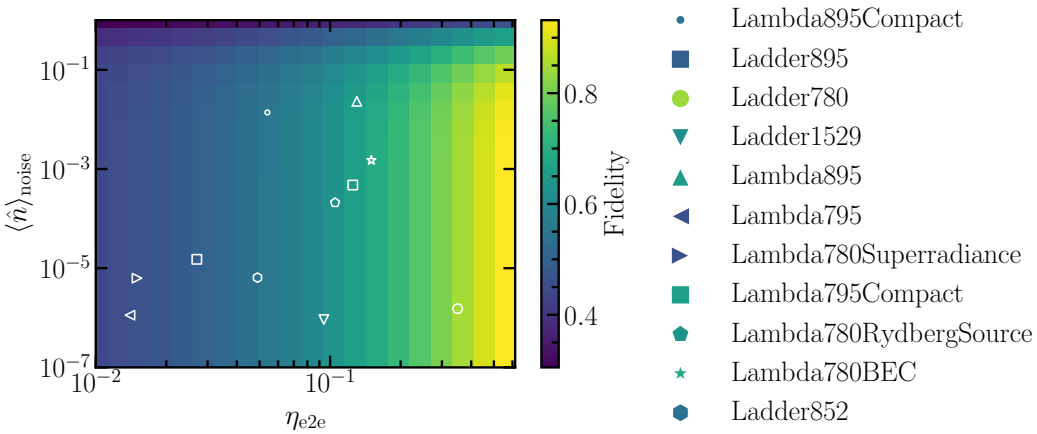

FIGURE B3 Simulated fidelity of different quantum memory experiments with and coherent state input $\alpha = 1$. The end-to-end efficiency has the highest influence on the fidelity of the retrieved state. In the experimentally achieved efficiency regime the number of noise photons doesn't influence the fidelity. Truncation $n = 5$.

TABLE 1 This table collects the re-trigger time, polarization acceptance and memory protocols of some of the most recent atomic vapor memories.

Reference	**Polarization**	**re-trigger time**	**memory protocol**	Remarks
Jutisz et al. (2025) [24]	linear	32.7 μs	λ-configuration (Raman EIT)	coherent states at single-photon level
Maaß et al. (2024) [36]	linear (V measured)	33 ns	ladder-configuration (FLAME)	coherent states at single-photon level
Davidson et al. (2023) [37]	circular (σ^+ measured)	108 ns	ladder-configuration (FLAME)	coherent states at single-photon level
Thomas et al. (2023) [38]	linear	12.5 ns	ladder-configuration (ORCA)	coherent states at single-photon level
Esguerra et al. (2023) [34]	linear	11 μs	λ-configuration (Raman EIT)	coherent states at single-photon level
Buser et al. (2022) [15]	circular (σ^- measured)	2.7 μs	λ-configuration (Raman EIT)	SPDC single photons
Rastogi et al. (2022) [39]	linear	5.7 μs *	λ-configuration (SR-mediated)	coherent states at single-photon level
Wang, Craddock et al. (2022) [31]	circular (σ^- measured)	5 ms	λ-configuration (Raman EIT)	coherent states at single-photon level
Heller et al. (2022) [40]	circular	11ms	λ-configuration (Raman EIT)	Lambda780RydbergSource
Saglamyurek et al. (2022) [41]	circular	20s	λ-configuration (ATS)	
Kaczmarkek et al. (2018) [42]	linear (H measured)	12.5 ns	ladder-configuration (ORCA)	SPDC single photons
Wei et al. (2020) [43]	circular (σ^+ measured)	n.a.	λ-configuration (Raman EIT)	coherent state at single-photon level
Vernaz-Gris et al. (2018) [44]	circular (σ^+ measured)	50 ms	λ-configuration (Raman EIT)	coherent states at single-photon level
Katz et al. (2018) [30]	linear (H measured)	n.a.	λ-configuration (Raman EIT)	coherent states

*This value does not include the preparation time of the cold ensemble which is on the order of ms.

TABLE 2 This table collects the performance metrics of some of the most recent atomic vapor memories.

Reference	**Atomic species**	**Wavelength [nm]**	**End-to-end efficiency** ($\tau_s = 0$)	μ_1	**Bandwidth**	**1/e Storage time**	Class name
Jutisz et al. (2025)[a] [24]	Cs	895	0.054 (0.23 internal)	0.06	> 44 MHz	2.4μs	Lambda895Compact
Maaß et al. (2024) [a] [36]	Cs	895	(0.027 (0.210 internal)	7.2×10^{-5}	560 MHz	32 ns	Ladder895
Davidson et al. (2023) [a] [37]	Rb	780	0.35 (0.51 internal)	3×10^{-6}	370 MHz	108 ns	Ladder780
Thomas et al. (2023)[a] [38]	Rb	1529	0.11 (0.21 internal)	4.4×10^{-6}	> 1 GHz	1.1 ns	Ladder1529
Esguerra et al. (2023)[a] [34]	Cs	895	0.13 (0.33 internal)	0.07	220 MHz	140 ns	Lambda895
Buser et al. (2022) [a] [15]	Rb	795	0.014 (0.047 internal)	2.4×10^{-5}	370 MHz	680 ns	Lambda795
Rastogi et al. (2022)[b] [39]	Rb	780	0.015[c] (0.03 internal)	2.1×10^{-4}	12.7 MHz	4.7 μs	Lambda780Superradiance
Wang, Craddock et al. (2022)[a] [31]	Rb	795	0.125[c] (0.25 internal)	1.9×10^{-3}	2 MHz	180 μs	Lambda795Compact
Heller et al. (2022) [b] [40]	Rb	780	0.105[c] (0.21 internal)	1.0×10^{-3}	17.6 MHz	1.2 μ s	Lambda780RydbergSource
Saglanyurek et al. (2021) [b] [41]	Rb	780	0.15[c] (0.3 internal)	5×10^{-3}	22 MHz	15.8μs	Lambda780BEC
Kaczmarkek et al. (2018) [a] [42]	Cs	852	0.049 (0.17 internal)	3.8×10^{-5}	1000 MHz	5.4 ns	Ladder852
Wei et al.(2020) [b] [43]	Cs	895	0.8 internal	n.a.	31.4 MHz	54μs	
Vernaz-Gris et al. (2018)[b] [44]	Cs	852	0.70 internal	n.a.	2 MHz	14 μs	
Katz et al. (2018)[a] [30]	Cs	895	0.09 internal	n.a.	n.a.	149 ms	

[a]Operated at room-temperature.
[b]Operated at cryogenic temperature.
[c]No value provided, calculated assuming $\eta_{\text{transm}} = 0.5$.
*Remark::*We do not provide fitting errors for the value of n_b because they are much smaller than the measurement errors of the SNR, which is not always provided in the literature. The given end-to-end efficiencies correspond to the extrapolated "zero time" efficiencies as it is convention in the community. We want to emphasize that the practical meaning of this measure is questionable as all memories will have lower efficiencies for any practical storage time.